Magnetic Resonance Materials in Physics, Biology and Medicine
https://doi.org/10.1007/s10334-025-01246-2

RESEARCH ARTICLE

Accuracies of four simulation approaches in reproducing motion artifacts and morphometric parameter biases

Bingbing Zhao[1] · Yichen Zhou[1] · Xiaopeng Zong[1,2]

Received: 27 November 2024 / Revised: 19 March 2025 / Accepted: 22 March 2025

Abstract

Objective Despite widespread uses in MRI research, the relative accuracies of different motion artifact simulation approaches in reproducing artifacts and artifact-induced changes (AIC) of morphometric parameters in structural MRI remain largely unknown. We aim to evaluate the performances of four simulation approaches in reproducing artifacts and AIC of brain morphometric parameters.

Methods Within-session repeated T_1-weighted scans were acquired on ten volunteers with their heads remaining still or undergoing intentional motion monitored by fat navigators. Four simulation approaches were adopted, which differed in terms of whether channel-combined magnitude image or complex multi-channel k-space data were utilized, and whether motion effects were introduced by modifying k-space data value (MDV) or modifying k-space coordinates and data phase (MCP). By means of simulation, the dependence of morphometric parameter changes on motion pattern and severity was studied.

Results Multi-channel k-space database simulation achieved higher artifact similarity and AIC consistency with measured motion scan images than magnitude image-based simulation. MDV- and MCP-based simulations achieved comparable results. From k-space database simulation employing MDV, the motion-induced biases in morphometric parameters were found to vary linearly with motion severity with motion pattern-dependent slopes.

Conclusions Simulations based on multi-channel complex k-space data outperformed those based on channel-combined magnitude images in reproducing artifacts and AICs. Head motion caused imaging artifacts and systematic biases in morphometric parameters which can be equally reproduced by simulations using two different motion effect introduction strategies.

Keywords Motion artifact simulation · Head motion · Morphometric parameter bias · Structural brain MRI

Introduction

Motion artifact simulation has multiple applications in MRI research, including generation of motion-corrupted images for training artifact reduction networks [1–5], evaluation of motion correction performance [6, 7], and illustration of motion effects on brain morphometric parameters [8, 9]. Despite its common use in MRI research, it remains unclear how well the motion effects in real images can be reproduced by artifact simulation. In cases with severe motion, Zahneisen et al. demonstrated that simulation based on artifact-free images acquired with prospective motion correction can reproduce artifacts that are visually similar to those in images without motion correction but with similar motion profiles [7]. However, the simulated motion severity was very high (rotational motion range > 10°). Therefore, it remains unclear whether the similarity would remain for less severe motion commonly encountered in routine MRI studies.

Motion introduces systematic biases into brain morphometric parameters [9–16]. Different motion artifact distribution between study groups could confound the interpretation of neuroimaging findings, particularly in populations with varying degrees and patterns of motion, such as those with neurodevelopmental or neurodegenerative disorders [15]. However, the dependence of morphometric

✉ Xiaopeng Zong
zongxp@shanghaitech.edu.cn

[1] School of Biomedical Engineering and State Key Laboratory of Advanced Medical Materials and Devices, ShanghaiTech University, 393 Middle Huaxia Road, Shanghai, China

[2] Shanghai Clinical Research and Trial Center, Shanghai, China

Published online: 11 April 2025

parameter changes on motion pattern remains largely unexplored. Similarity between simulated and real images would allow us to use motion artifact simulation to estimate the motion effects on morphometric parameters so as to eliminate motion-induced biases in brain morphometric-related studies. However, it is unclear whether the motion effects on morphometric parameters, such as cortical thickness and gray matter volume derived from real images, are the same as those derived from images simulated using the same motion profiles.

Multiple methods have been proposed for performing motion artifact simulation, including those utilizing channel-combined magnitude images [3–6, 8, 17] and those utilizing multi-channel complex k-space data [2, 7, 18]. As complex k-space data are often not available and simulations using multi-channel complex k-space data are computationally much more expensive than those based on magnitude images, magnitude image-based approaches are preferred if they can be demonstrated to produce similar results. Furthermore, motion effects were introduced in these simulations either (1) by modifying k-space coordinates (for rotational motion) and data phase (for translational motion), and then obtaining the final image by inverse non-uniform Fourier transform [7], or (2) by modifying k-space data value by non-uniform Fourier transform according to different head orientations and obtaining the final image by inverse Fourier transform [6]. It is unclear whether the different approaches can produce similar artifacts and image metrics. These two approaches will be referred to as MCP (modification of coordinate and phase) and MDV (modification of data value), respectively.

In this study, we aim to evaluate the accuracies of different simulation strategies in reproducing artifacts and artifact-induced changes (AIC) of morphometric parameters in T_1-weighted structural brain MRI images, and to determine the dependence of AIC on motion pattern and severity.

Methods

Data acquisition

Images were acquired on a 3T uMR890 MRI scanner (United Imaging, Shanghai, China) equipped with a 2-channel transmit coil and a 64-channel receive coil. The T_1-weighted inversion-recovery gradient echo sequence was used with the following parameters: TR/TE/TI = 2400/2.3/1000 ms, flip angle = 8°, voxel size = 0.8 × 0.8 × 0.8 mm^3, matrix size = 320 × 300 × 208, field of view (FOV) = 256 × 240 × 166.4 mm^3, 20% oversampling along the partition encoding (PAR) direction. No partial Fourier acceleration was performed along the phase encoding (PE) or PAR directions. The k-space was fully sampled in the central region with a size of 25 × 25, but was randomly undersampled with probabilities of 0.348 and 0.254 in the outer regions defined as (1) $|k_{pe}| \leq 0.673k_{pe,max}$ and $|k_{par}| \leq 0.806k_{par,max}$, and (2) $|k_{pe}| > 0.673k_{pe,max}$ or $|k_{par}| > 0.806k_{par,max}$, respectively, resulting in a total undersampling factor of 3.2 [19]. The sampling pattern is shown in Fig. S1.

The 3D fat navigator (FatNav) [20] was embedded into each TR to monitor head movements with the following sequence parameters: TR/TE = 4.7/2.3 ms, flip angle = 7°, voxel size = 4 × 4 × 4 mm^3, matrix size = 56 × 56 × 56, FOV = 224 × 224 × 224 mm^3, undersampling factor R = 4 × 4 and partial Fourier factor = 0.8 along both PE and PAR directions. A FatNav image with fully sampled rectangular region around k-space center was acquired before the first TR for obtaining the calibration data for GRAPPA [21] reconstruction. The FOV center of FatNav coincided with that of the main image.

The study was approved by the Institutional Review Board at ShanghaiTech University. Ten healthy volunteers (aged 19–46 years, 6 males) were enrolled in this study after obtaining informed consent. All the subjects underwent two scans within the same imaging session, one in which they were instructed to remain as still as possible (referred to as "still scan"), and the other in which they were instructed to perform intentional movements (referred to as "motion scan"). Apart from the suggestion to move head every 30 s, no specific motion type or motion severity was instructed in order to encompass a wide range of motion scenarios. Among the ten subjects, two underwent the scanning session twice on two different days, resulting in a total of twelve paired images with and without motion.

Motion artifact simulation

To investigate whether simulations based on magnitude images or complex k-space data, and whether different motion introduction strategies, i.e., MCP and MDV, can produce results that are more similar to real motion artifacts, four different motion simulation approaches were adopted. Their differences are shown in Fig. 1. Either channel-combined magnitude image (Approaches 1–2) or complex multi-channel k-space data (Approaches 3–4) of still scans were used. Approaches 1 and 3 adopt MDV according to different head orientations, place these motion-corrupted k-space data into the intended Cartesian coordinates, and obtain the final image using inverse fast Fourier transform (FFT) as shown in Fig. 1B. In contrast, Approaches 2 and 4 adopt MCP by moving the measured k-space data into non-Cartesian grid to account for motion effects, and obtain the final image using inverse non-uniform fast Fourier transform (NUFFT), as shown in Fig. 1C. We note that, despite being labeled as MCP, the interpolated k-space data at the Cartesian grid in Approaches 2 and 4, which are generated

(A)

	MDV	MCP
Magnitude image	Approach 1	Approach 2
Multi-channel k-space data	Approach 3	Approach 4

(B)

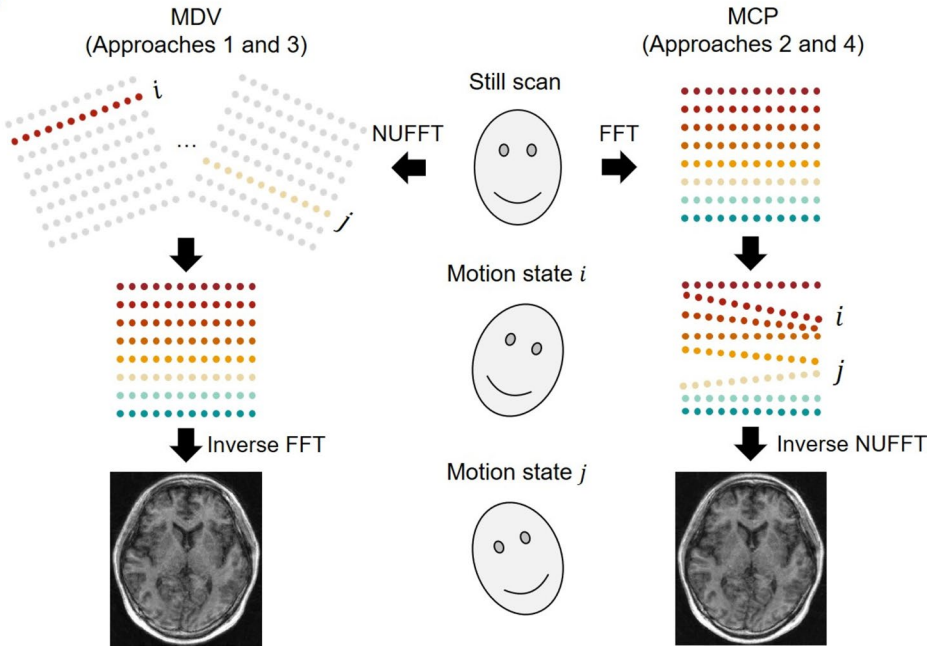

Fig. 1 **A** Differences between four motion artifact simulation approaches. **B** Diagram of two motion effect introduction strategies. MDV modifies k-space data values of still scan according to different motion states by non-uniform fast Fourier transform (NUFFT), places the motion-corrupted data into Cartesian grid and obtains the image by inverse fast Fourier transform (FFT). MCP modifies k-space coordinates and data phases of still scan into non-Cartesian grid and obtains the image by inverse NUFFT. Different colors represent k-space lines acquired at different TR. Assuming that the motion parameters vary between TRs, the colored k-space lines all have different orientations. In each motion state, gray indicating unused data during that TR

during inverse NUFFT, are also different from the original data. However, the motion effects have been introduced in the MCP step before interpolation. The detailed steps for each approach are described as follows and shown in Fig. S2.

Approach 1: This approach adopts MDV based on magnitude images. It was developed in our earlier study [6], and includes the following steps: (1) the magnitude image is expanded by zero padding to account for oversampling along PAR direction such that its Fourier transform matches the sampled k-space positions. (2) The rotational motion parameters are applied to the Cartesian k-space coordinates k to obtain the real measured non-Cartesian k-space coordinates $k\prime$ by $k\prime = Ak$, where A is the rotation matrix that brings the moved head position back to the original orientation. Then the expanded image is transformed to obtain the k-space data $S\prime(k\prime)$ at coordinates $k\prime$ through 3D NUFFT [22], where the apostrophe indicates modification by motion. Due to undersampling, motion parameters for unsampled k-space positions are assigned to be the same as those of the nearest sampled positions. (3) The k-space data at $k\prime$ are placed onto the predefined Cartesian coordinates k and the corresponding phase is adjusted according to $S\prime(k) = S\prime(k\prime) \bullet e^{ik\bullet\Delta r}$ to account for the linear phase shift due to translational motion, where Δr is the translational motion parameter that brings the moved head back to its original position. (4) Apply inverse FFT (iFFT) of $S\prime(k)$ followed by cropping the voxels added during step (1) to obtain the final image.

Approach 2: This approach adopts MCP based on magnitude images and includes the following steps: (1) expand the image matrix by zero padding. (2) The expanded image is transformed into k-space through 3D FFT. (3) Assign motion parameters to unsampled k-space positions using the same method as in Approach 1. Then, modify the k-space coordinates according to $k\prime = A^{-1}k$, place the k-space data from step (2) onto the transformed coordinates $k\prime$, and finally adjust the corresponding phase according to $S\prime(k\prime) = S(k) \bullet e^{ik\prime\bullet\Delta r}$. We note that the inverse matrix of A is used in coordinate transform in this approach, such that the directions of relative mismatch between k-space data and k-space coordinates remain the same between Approaches 1 and 2. (4) Apply inverse NUFFT of $S\prime(k\prime)$ followed by cropping the voxels added during step (1) to obtain the final image.

Approach 3: This approach adopts MDV based on multi-channel complex k-space data and includes the following steps: (1) SPIRiT [23] reconstruction algorithm is employed to reconstruct the undersampled k-space data into multi-channel image data. SPIRiT fills the unsampled k-space data along PE and PAR directions at each readout (RO) coordinate. The data are now in the image space along PE and PAR directions, and then the multi-channel image data

are obtained after iFFT along RO direction. (2)–(3) Follow the same steps as (2)–(3) in Approach 1 but deal with multi-channel data. (4) Apply iFFT and coil combination by square root of the sum of squares (SOS) to obtain the final image.

Approach 4: This approach adopts MCP based on multi-channel complex k-space data, which was first proposed by Zahneisen et al. [7], and includes the following steps: (1) modify the k-space coordinates and phase according to $k\prime = A^{-1}k$ and $S\prime(k\prime) = S(k) \bullet e^{ik\prime \bullet \Delta r}$. Different from Approaches 1–3, the motion parameters are only applied to the sampled k-space data and coordinates, thus avoiding the need for motion parameter interpolation. (2) Perform interpolation on k-space coordinates so that all the measured k-space lines have the same RO coordinates, which is accomplished by first performing iFFT along the k-space line, second adding linear phase shifts $e^{-i\delta k \bullet x}$, where δk is the k-space coordinate shift caused by motion and x is the coordinate along the motion-modified RO direction, third performing FFT along the same direction. (3) Perform SPIRiT at each plane with the same RO coordinate to fill the unsampled k-space data. The SPIRiT step is similar to step (1) in Approach 3 but involves NUFFT since the PE and PAR coordinates are no longer on the Cartesian grid. (4) Perform iFFT along RO direction and coil combination by SOS to obtain the final image.

To determine the capability of our algorithms in reproducing motion artifacts and AICs of morphometric parameters, we used the motion profile from motion scan and the artifact-free image from still scan of the same subject to simulate the artifacts manifested on motion scan images. Simulation Approaches 1–4 with such a method for selecting motion profiles will be referred to as Simu 1–4. Since only motion scan images are usually available in clinical setting, one can also utilize the motion profile to simulate artifacts using an existing artifact-free image from a different subject to obtain the AIC. Therefore, we also used the motion profile and the artifact-free image from two different subjects to simulate the artifacts. Such simulations will be referred to as dSimu 1–4. Notably, the simulated AIC for Simu and dSimu were originated from the same motion profile, and differed in that the baseline and simulated images of dSimu came from a subject different from Simu.

To explore the relationship between AIC and motion severity, three representative subjects with distinct motion patterns were chosen to simulate motion artifacts and calculate AIC using Simu 3. The motion profiles are shown in Figs. 2, 3, and 4 and represent step-wise, random, and peak-wise motion patterns, respectively. For each motion type, the motion pattern was maintained, but the rotation and the translation amplitudes were scaled into eight different levels with motion scores of 1.8 mm, 2.9 mm, 3.9 mm, 5.0 mm, 6.1 mm, 7.1 mm, 8.1 mm and 9.1 mm as shown in Figs. S3–S5.

The simulations were implemented in MATLAB R2021a (The MathWorks, Natick, MA, USA) and Approaches 1, 2, 3, and 4 took an average of 6 min, 6 min, 25 h, and 13 h on a computer equipped with 3.3 GHz Intel Xeon W-2275 CPU, respectively.

Data processing and analysis

Image reconstruction

The T_1-weighted images of still and motion scans were reconstructed using the same SPIRiT algorithm [23] as in Approaches 3 and 4, without applying the motion parameters. The FatNav images were reconstructed using GRAPPA [21] algorithm.

Motion parameters

The motion profile of each subject was obtained by registering the FatNav images to the reference FatNav image acquired at the 47th TR using the 3dvolreg tool in AFNI [24]. The 47th FatNav image was chosen as the reference since the k-space center of T_1-weighted image was acquired during this repetition. Each motion profile contained a series of rotational and translational motion parameters around or along left–right (L–R), anterior–posterior (A–P) and superior–inferior (S–I) spatial directions.

To determine the estimated accuracy of FatNav motion detection, the time series of motion parameters was split into segments of slow drifting periods and then fitted with piecewise second-order polynomial. The residual variance of each segment after the fit was calculated and averaged to obtain the residual standard deviation (rSD) which served as an estimate of the random fluctuations of motion parameters [25].

The motion severity was quantified using motion score [25], which was calculated as a combination of translational (M_T, unit: mm) and rotational motion ranges (M_R, unit: radian) over the whole scan given by: motion score $= M_T + 57.3\text{mm} \times M_R$. The motion ranges were defined as the root sum square of the differences between the maximum and the minimum values of the rigid body motion parameters. The radius of 57.3 mm is chosen in Ref. [25] of Zong et al., such that the motion score can be simply calculated as the sum of translational and rotational motion ranges in units of mm and degrees, respectively. Alternatively, Tisdall et al. [26] computed the motion score for motion between two neighboring TRs as the sum of translations and the maximum shift caused by rotations of a point on a sphere with a radius of 64 mm. The maximum motion score over all TRs will be referred to as $MS_{Tisdall}$ to distinguish it from the motion score defined in Ref. [25] which will be referred to simply as motion score.

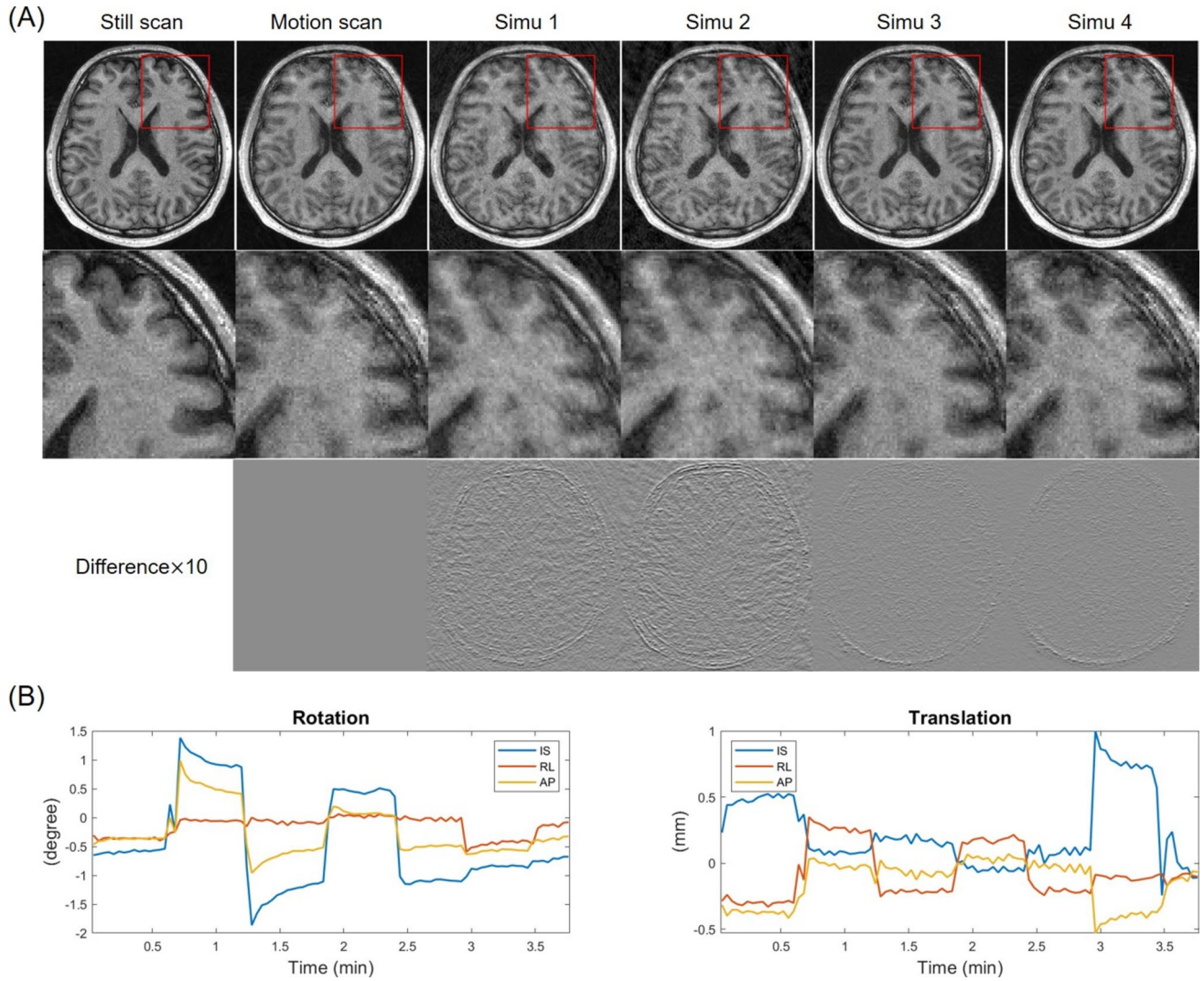

Fig. 2 Representative still scan, motion scan, and simulated images for step-wise motion. **A** From left to right, upper panels are still scan, motion scan, and simulated (Simu 1–4) images, respectively. Middle panels are zoomed images of regions marked with red rectangles, respectively. Lower panels are differences between the simulated and motion scan images scaled by a factor of 10. **B** Motion profile of motion scan. The motion score and $MS_{Tisdall}$ are 5.37 mm and 2.64 mm, respectively

Brain morphometric parameters

Two voxel-based brain morphometric parameters were extracted using the segmentation algorithm [27] in SPM12, including gray matter (GM) and white matter (WM) volume. The GM and WM volumes were calculated by multiplying the voxel size and the number of segmented voxels from the tissue probability maps with a threshold of 0.5. Prior to segmentation, B_1 bias field correction was performed. The SPM parameters were set as follows: the cut-off full width at half maximum of Gaussian smoothness of bias field was set to 50 mm. The numbers of Gaussians used to represent the intensity distribution for GM, WM and cerebrospinal fluid were 2, 2, and 3, respectively. The "thorough clean-up" option in SPM segmentation algorithm was used to remove non-brain voxels.

The AIC of GM and WM volumes was calculated as the percent volume difference of motion-affected images from still scan images.

Image similarity and artifact metrics

To assess image similarity of still scan and simulated images with measured motion scan images, structural similarity index measure (SSIM) and peak signal-to-noise ratio (PSNR) within GM and WM were calculated. The still scan, motion scan and simulated images all underwent bias field correction. Then the still scan and simulated images were registered to the corresponding motion scan image using

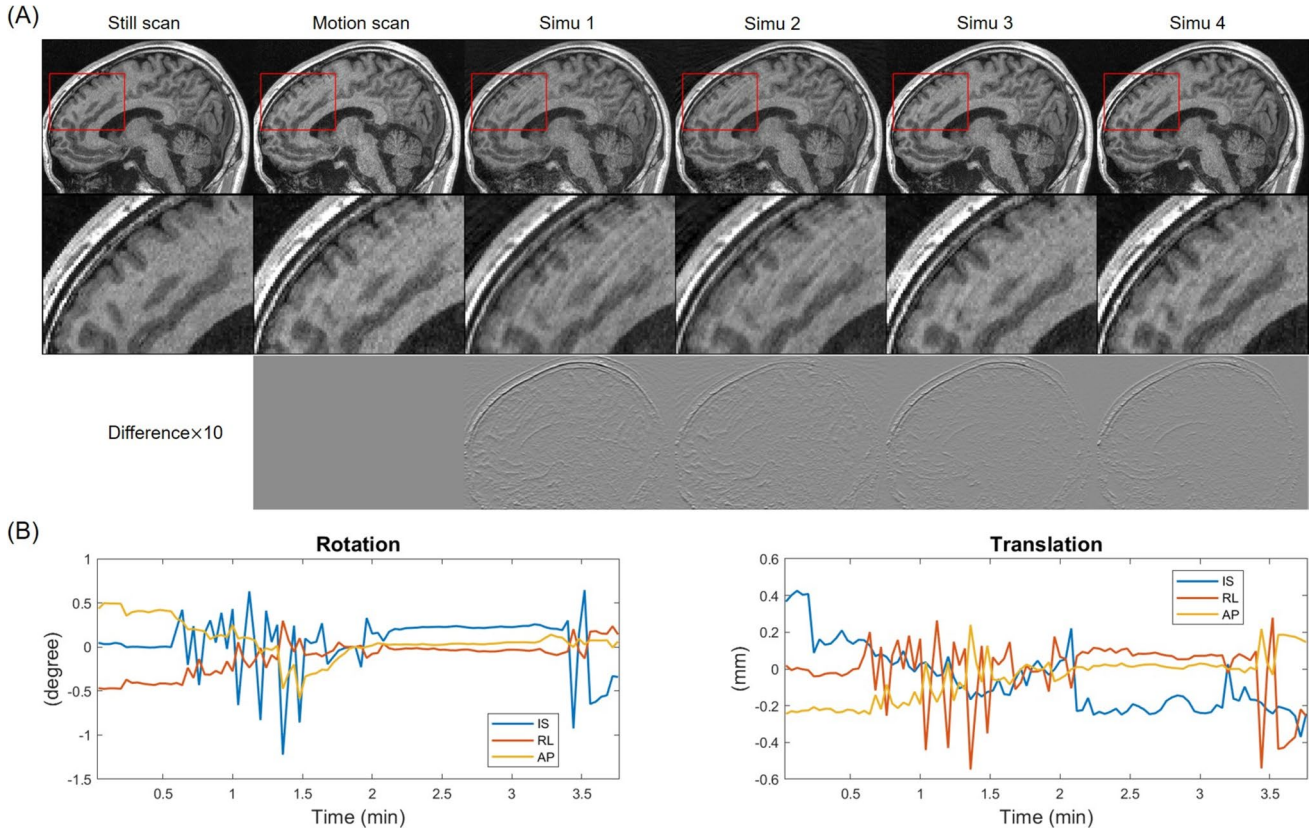

Fig. 3 Representative still scan, motion scan, and simulated images for random motion. **A** From left to right, upper panels are still scan, motion scan, and simulated (Simu 1–4) images, respectively. Middle panels are zoomed images of regions marked with red rectangles, respectively. Lower panels are differences between the simulated and motion scan images scaled by a factor of 10. **B** Motion profile of motion scan. The motion score and $MS_{Tisdall}$ are 3.54 mm and 2.12 mm, respectively

co-register algorithm [28] in SPM12 with the 4th B-Spline interpolation to minimize voxel mismatches due to head motion and ensure smooth transitions between voxels so as to maintain anatomical and artifact fidelity. Intensity normalization was applied to ensure overall intensity consistency across different images. Blurriness at lateral ventricle-WM boundary was calculated as the full width at half maximum (FWHM) of an edge function fitted to the scatter plot of intensity versus distance to the boundary plane of all voxels within the region of interest (ROI) [29]. The ROI was a cuboid across the boundary with a size of 4 (R-L) × 8 (A-P) × 6 (S-I) mm^3. The contrast-to-noise ratio between GM and WM ($CNR_{GM/WM}$) was used to measure the artifact-induced intensity variations on brain tissue, which was calculated as the ratio of the mean GM and WM intensity difference to the square root of the sum of signal variances within GM and WM after correcting intensity inhomogeneity in SPM12. The GM and WM masks were the same as those used to obtain morphometric parameters. The background noise level ($Noise_{bg}$) was calculated as the standard deviation of intensities within 24-mm-wide squares at the four corners of all axial slices.

To quantify the artifact discrepancy between simulated and real motion scan images, the artifact difference was quantified by their mean squared voxel-wise intensity difference subtracted by noise variance. A first-order polynomial was used to fit the intensity within an ROI located in homogeneous WM in the still scan images with a size of 8 (R-L) × 8 (A-P) × 8 (S-I) mm^3. Then the mean squared fitting residual was used to represent the noise variance on both still scan and motion-affected images.

Statistical analysis

The motion scores of still and motion scans were not normally distributed (Shapiro–Wilk test; $p \leq 1.5 \times 10^{-4}$). Statistical difference of motion scores between the still and motion scans was assessed with Wilcoxon signed-rank test. Analysis of variance (ANOVA) and post hoc Tukey–Kramer tests were performed to identify significant differences in image metrics between different simulation approaches. Wilcoxon signed-rank test with Bonferroni correction was performed to identify significant difference in the image metrics of still scan and simulated images

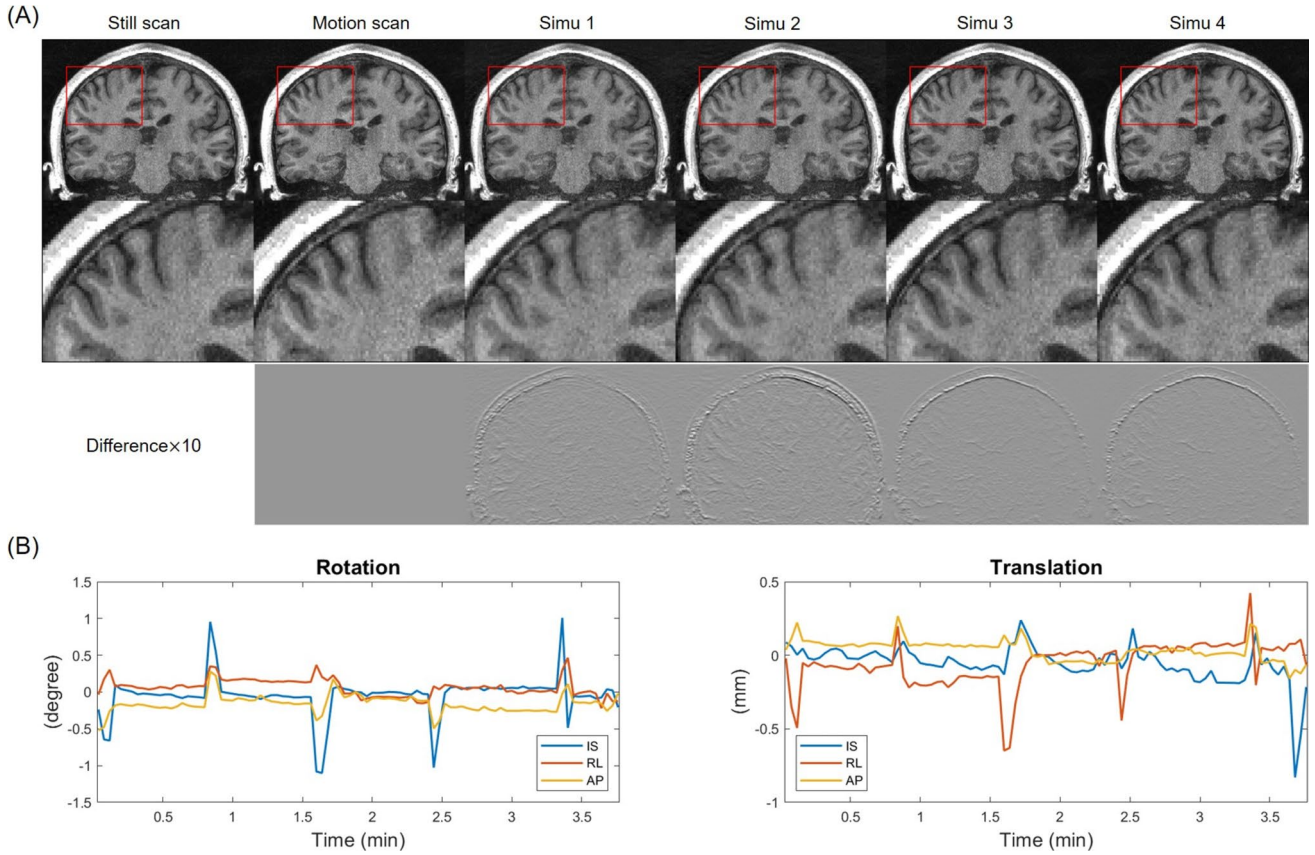

Fig. 4 Representative still scan, motion scan, and simulated images for peak-wise motion. **A** From left to right, upper panels are still scan, motion scan, and simulated (Simu 1–4) images, respectively. Middle panels are zoomed images of regions marked with red rectangles, respectively. Lower panels are differences between the simulated and motion scan images scaled by a factor of 10. **B** Motion profile of motion scan. The motion score and $MS_{Tisdall}$ are 3.93 mm and 2.02 mm, respectively

compared to motion scan image. The measured GM and WM volumes followed normal distribution (Shapiro–Wilk test; $p \geq 0.11$). Pearson's correlation test was performed to study the relationship between measured and simulated AICs and motion score. The consistency between measured and simulated AIC was analyzed using Lin's concordance correlation coefficient (CCC) and mean absolute error (MAE) after excluding outliers. The outliers were identified as points that fell outside the lines representing the 95% confidence interval for the mean difference. The significance threshold of p values was set to 0.05.

Results

Capability of simulation in reproducing motion artifacts

Figure S6 presents the estimated accuracy of FatNav motion parameters across all motion scans. The maximum rSDs were 0.070° for rotation around the RL axis and 0.067 mm for translation along the IS axis, respectively. The means and the standard deviations of rSDs for rotation around the IS, RL and AP axes were 0.022°± 0.011°, 0.032°± 0.014°, and 0.030°± 0.011°, respectively. The means and the standard deviations of rSDs for translation along the IS, RL and AP axes were 0.037 ± 0.012 mm, 0.026 ± 0.011 mm, and 0.033 ± 0.009 mm, respectively.

The motion scores of still and motion scans had ranges of 0.51 mm–2.37 mm (0.91 ± 0.48 mm), and 1.92 mm–12.14 mm (5.48 ± 2.93 mm), respectively, which were significantly different from each other (Wilcoxon signed-rank test; $p = 9.77 \times 10^{-4}$), as shown in Fig. S7A. The mean values and the standard deviations of $MS_{Tisdall}$ of still scans and motion scans were 0.53 ± 0.31 mm and 3.94 ± 2.77 mm, respectively, which also showed a significant difference (Fig. S7B). The motion scores were higher than $MS_{Tisdall}$. However, they exhibited strong correlations as shown in Fig. S7C (Spearman's test; ρ=0.98, $p = 2.08 \times 10^{-6}$), suggesting that both motion scores can reflect motion severity.

The motion patterns of all the motion scans were classified into step-wise, random, and peak-wise, and the numbers of scans in the three categories were 7, 2, and 3, respectively. Figures 2, 3, and 4 show the representative motion profiles and images for step-wise, random, and peak-wise motion, respectively. As visualized in the zoomed images, image-based approaches (Simu 1–2) generated more severe blurring and ringing artifacts at GM/WM boundary compared to the motion scans, resulting in relatively lower SSIM and PSNR. On the contrary, Simu 3–4 reproduced artifacts that were most similar to motion scan and exhibited the lowest intensities in the difference images for all motion types.

The boxplots in Fig. 5A compare the image metrics of still scan, motion scan and simulated images. Their mean values are shown in Fig. 5B. The k-space-based approaches (Simu 3–4) exhibited overall higher similarity to the real motion scans in GM and WM (SSIM $\geq$ 0.85; PSNR $\geq$ 31.60) compared to the magnitude image-based approaches (Simu 1–2) (SSIM $\leq$ 0.81; PSNR $\leq$ 28.86) although only the PSNR differences between Simu 3–4 and Simu 2 reached significance (ANOVA; corrected $p \leq 0.03$). There was no significant difference between Simu 1 and 2 or between Simu 3 and 4 (ANOVA; corrected $p \geq 0.97$) in SSIM or PSNR. The blurriness and $CNR_{GM/WM}$ between still and motion scans exhibited significant difference (Wilcoxon signed-rank test; corrected $p \leq 0.002$). Compared to Simu 1–2 and still scans, Simu 3–4 were closer to the motion scan in terms of blurriness and $CNR_{GM/WM}$ although there were still significant differences between Simu 3–4 and motion scan in $CNR_{GM/WM}$. All simulations resulted in significantly higher $Noise_{bg}$ compared to the motion scans, especially for Simu 1–2, which was also visible in the difference images in Figs. 2A, 3A and 4A.

Figure 6 shows the relative artifact difference within GM and WM of still scan and simulated images compared to motion scan image. Simu 3–4 can account for 23.18% of artifact variance within GM (Wilcoxon signed-rank test; corrected $p \leq 0.04$), and 11.79% of artifact variance within WM, which was measured by the mean squared difference between still scan and motion scan image intensities in GM and WM. On the contrary, Simu 1–2 exhibited larger artifact difference from motion scan than still scan and Simu 3–4.

Capability of simulation in reproducing AIC

Figure 7 shows the correlations of AIC between simulated (Simu 1–4) and motion scan images. Among the four simulation approaches, Simu 3 achieved the overall highest consistencies (CCC $\geq$ 0.86) and the lowest errors (MAE $\leq$ 0.009) for both GM and WM volumes. The magnitude image-based approaches (Simu 1–2) exhibited much lower CCC and higher MAE, except for the highest consistency achieved by Simu 2 for WM volume.

Figure 8 shows the correlations of AIC between dSimu and motion scan images. The dSimu and motion scan images for each data point had the same motion profile, but the subject for dSimu was different from that for the

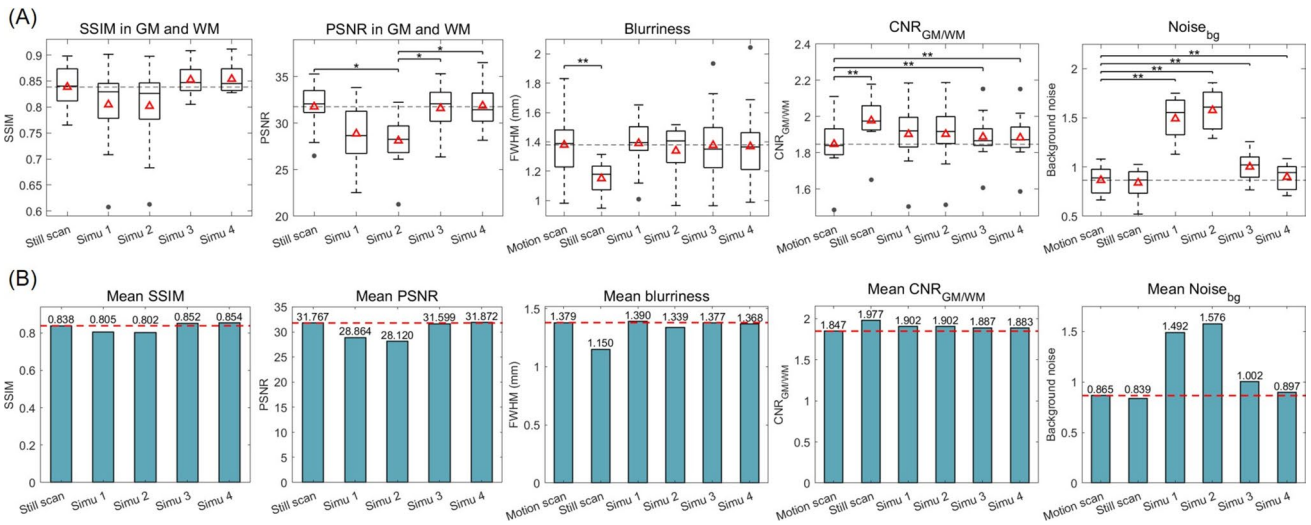

Fig. 5 Comparison of image metrics in four motion artifact simulations (Simu 1–4). **A** Boxplots of SSIM, PSNR, blurriness, contrast-to-noise ratio between gray and white matter ($CNR_{GM/WM}$) and background noise ($Noise_{bg}$). SSIM and PSNR were calculated relative to the real motion scan image. Black dashed lines represent the mean values of still or motion scans. Red triangle represents the mean value of each approach. ANOVA with Tukey–Kramer correction was performed in the first two columns and Wilcoxon signed-rank tests with Bonferroni correction were performed between motion scan and still scan/Simu in the last three columns. $*p < 0.05$, $**p < 0.01$. The pairs that do not show significant difference are not marked. **B** Mean values of image metrics. Red dashed line indicates the mean value of still or motion scan

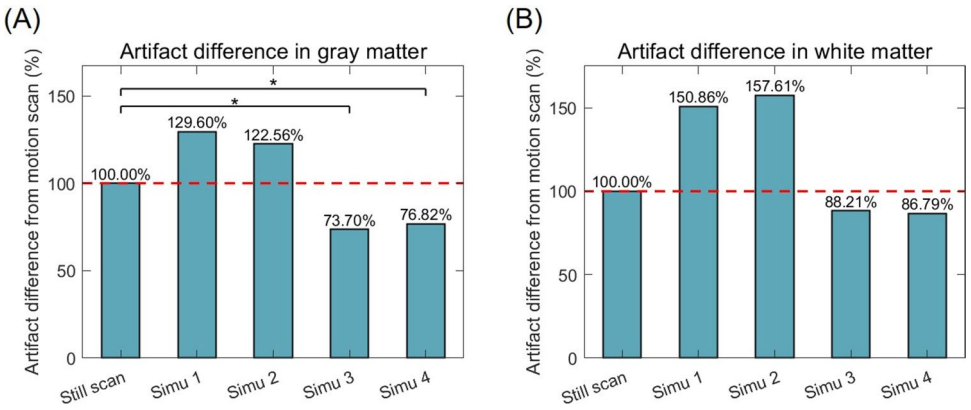

Fig. 6 Comparison of artifact differences within gray and white matter of still scan and simulated images compared to motion scan images. The relative artifact difference was calculated by the ratio of the mean squared difference between Simu 1–4 and motion scan to the mean squared difference between still and motion scans in (A) gray matter and (B) white matter. Red dashed line indicates the value of still scan. Wilcoxon signed-rank test was performed between still scan and Simu 1–4 with Bonferroni correction. $*p < 0.05$

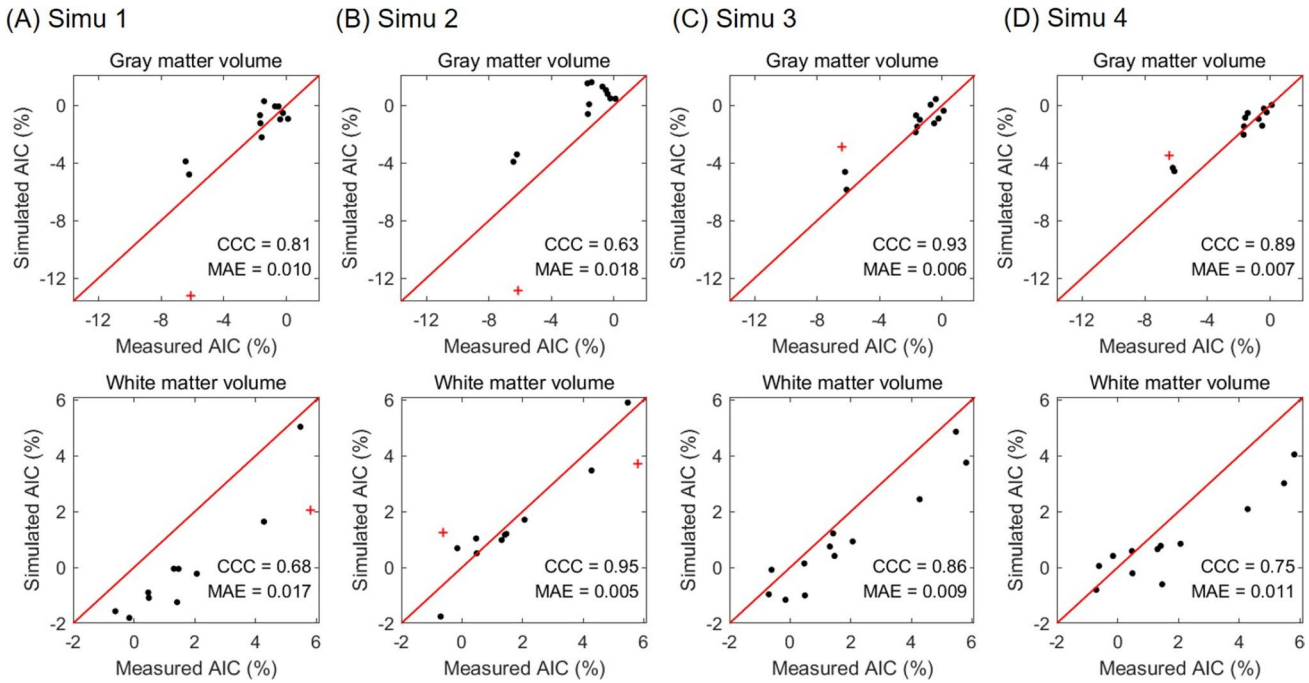

Fig. 7 Comparison of correlations between simulated and measured artifact-induced changes (AIC) in four motion artifact simulations (Simu 1–4) (A-D). Simulated and measured AICs represent the percent volume changes of simulated and motion scan images compared to the still scan images. Red lines denote identity lines. Red pluses denote outliers that fall outside the lines representing the 95% confidence interval for the mean difference. Lin's concordance correlation coefficient (CCC) and mean absolute errors (MAE) are shown after excluding the outliers

motion scan image. Consistencies between simulated and measured AIC were the strongest for dSimu 3 (CCC ≥ 0.64; MAE ≤ 0.013). However, all CCC of dSimu were lower than those of Simu especially for WM volume.

Relationships between AIC and motion score

Figure 9 shows the relationship between the measured AIC of motion scan and motion score for all subjects. A

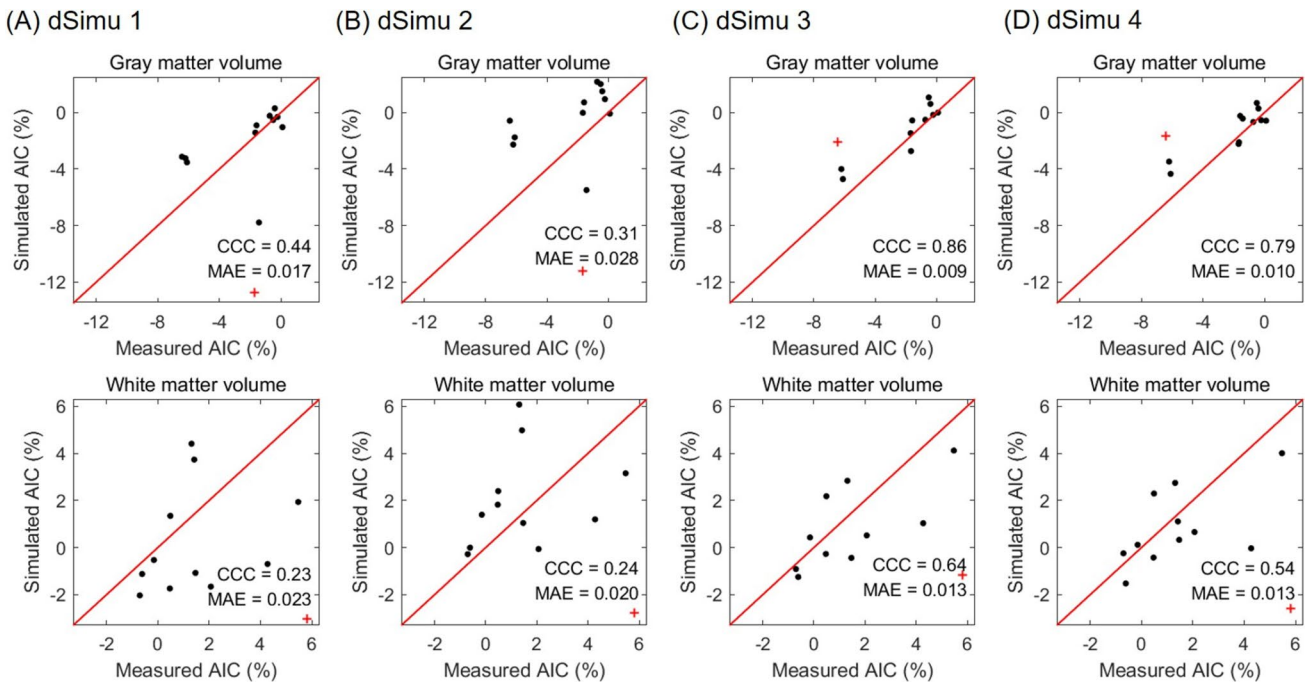

Fig. 8 Comparison of correlations between simulated and measured artifact-induced changes (AIC) in four motion artifact simulations (dSimu 1–4) (A-D). Simulated and measured AICs represent the percent volume changes of simulated and motion scan images compared to the still scan images. For each data point, the measured and the simulated AICs were originated from the same motion profile, but the AIC of dSimu was calculated on a subject different from the subject for measured AIC. Red lines denote identity lines. Red pluses denote outliers that fall outside the lines representing the 95% confidence interval for the mean difference. Lin's concordance correlation coefficient (CCC) and mean absolute errors (MAE) are shown after excluding the outliers

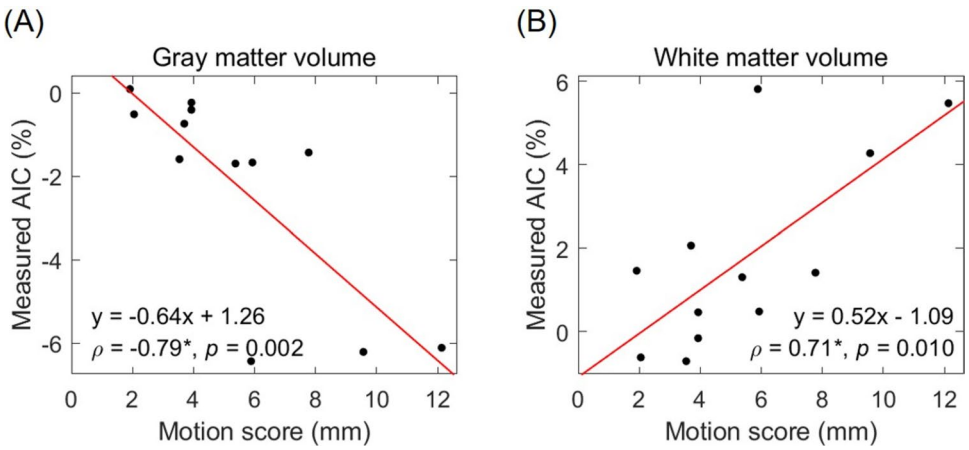

Fig. 9 Correlations between the measured artifact-induced change (AIC) of **A** gray matter volume and **B** white matter volume and motion score. The measured AIC represents the percent parameter change between the motion scan and still scan images. Coefficients and p values for Pearson's correlation test are shown, where asterisks denote significance ($p < 0.05$)

significant negative correlation was observed in GM volume (Pearson's test; ρ=-0.79, $p = 0.002$), and a significant positive correlation was observed in WM volume (Pearson's test; $\rho = 0.71$, $p = 0.010$). Such significant correlations were also found but weaker when using $MS_{Tisdall}$ as shown in Fig. S8.

Figure 10 shows the relationships between simulated AIC and motion score for step-wise, random, and peak-wise motions, respectively. For each motion type, the simulated AIC and motion scores were originated from the same motion pattern but with scaled motion parameters. The scaled motion profiles for step-wise, random, and peak-wise motions are shown in Figs. S3–S5, respectively. Significant correlations were found for all motion types (Pearson's test; $p \leq 0.002$), suggesting a linear relationship between the AIC and motion score within the range of 1.8–9.1 mm across different motion scenarios. The non-zero intercepts may indicate a potential non-linear relationship in cases with small motion (motion score < 1.8 mm).

The motion profile with the same motion score but different patterns resulted in different directions of morphometric

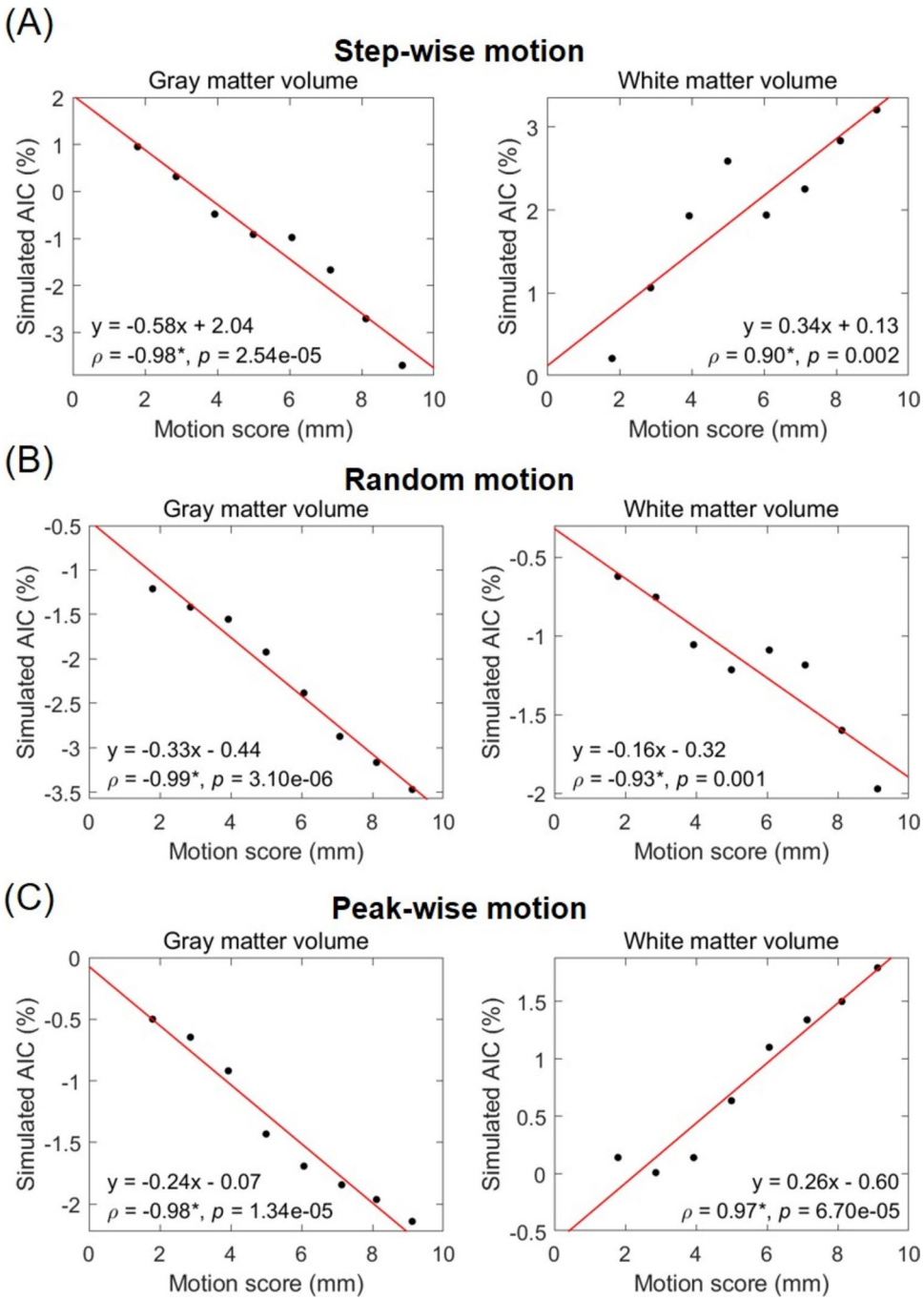

Fig. 10 Correlations between the simulated artifact-induced change (AIC) of gray matter and white matter volumes and motion score for **A** step-wise motion, B random motion, and **C** peak-wise motion, respectively. The simulated AIC represents the percent parameter change between Simu 3 and still scan image. For each motion type, the simulated AIC and motion scores were originated from the same motion pattern but with scaled motion parameters, whose motion scores were set to 1.8 mm, 2.9 mm, 3.9 mm, 5.0 mm, 6.1 mm, 7.1 mm, 8.1 mm and 9.1 mm. The scaled motion profiles for step-wise, random, and peak-wise motions are shown in Figs. S3–S5, respectively. Coefficients and p values for Pearson's correlation test are shown, where asterisks denote significance ($p < 0.05$)

parameter changes. As motion score increased from 1.8 mm to 9.1 mm, the WM volume significantly increased by 2.99% and 1.65% in the case of step-wise and peak-wise motion (Fig. 10A and C), while significantly decreased by 1.35% in the case of random motion (Fig. 10B).

Discussion

In this study, we compared four motion artifact simulation approaches in reproducing motion artifacts and AIC in

brain morphometric parameters. We found the superior performance of multi-channel complex k-space database simulations (Simu 3–4) over the magnitude image-based simulations (Simu 1–2) in both artifact similarity and AIC consistency with motion scans. The simulations with different motion introduction strategies (MDV and MCP) achieved comparable results. By means of simulation, we found that motion systematically biased the morphometric measurements in a motion pattern-dependent manner.

Currently, the motion artifact simulation approaches are categorized by the domain in which the motion effects are introduced [30]. The proposed approaches Simu 1–4 all introduce motion effects in k-space. Another popular simulation approach is introducing motion effects in image domain based on the coil-combined magnitude image [1, 4, 5, 8, 17], which is performed by rigidly transforming the magnitude image, concatenating the corresponding k-space lines of the Fourier transform of the transformed images, and obtaining the final image by iFFT. Simu 1 that adopts MDV based on magnitude image is similar to simulation in image domain. The k-space data obtained with Fourier transform of the object after space transformation are equivalent to the data obtained with MDV, except for some likely difference resulting from different numerical approaches adopted for interpolation during space transformation versus NUFFT.

The multi-channel k-space database simulation approaches (Simu 3–4) achieved overall higher similarity to the motion scans than the magnitude image-based approaches (Simu 1–2) (Fig. 5). Although Simu 1–2 entails much lower computational cost, they generated more severe blurring and ringing artifacts at GM/WM boundary and higher background noise than Simu 3–4. The superior performance of Simu 3–4 may be related to the fact that the multi-channel k-space data retain phase and coil sensitivity information, which enables more realistic simulation of motion artifacts.

On the other hand, the image similarity metrics between the simulations that introduced motion effects by MDV (Simu 1 and 3) and MCP (Simu 2 and 4) did not reach significant difference. This suggests that both approaches have similar performance in reproducing artifacts although the modification of k-space data without changing the k-space coordinates in Simu 1 and 3 matches more closely to the actual data sampling and image reconstruction process in the presence of motion [6]. Furthermore, in contrast to Simu 1–3, Simu 4 did not require artificial assignment of motion parameters for unsampled k-space positions.

Both MDV (Simu 3) and MCP (Simu 4) achieved lower artifact differences from the motion scan images than the still scan images (Fig. 6). However, the reductions in mean squared difference were less than 27% and 14% of the artifact variance in GM and WM, respectively. The residual differences may suggest the presence of other motion artifact mechanisms that were not considered in simulation, such as motion-induced coil sensitivity map [31, 32] and B_0 field changes [33, 34].

We found a linear relationship between the simulated AIC and the motion score (Fig. 10) for a given motion pattern. An earlier study [11] has found a linear relationship between GM volume and severity of real intentional motion, consistent with our findings. Our study conducted the simulations based on three distinct motion patterns (step-wise, random, and peak-wise motion) at eight motion severities. While the motion scores were kept consistent across different motion patterns, the variations in their resulting AICs were noteworthy. The directional changes of AIC suggest that motion induces a systematic bias in morphometric measurements, rather than simply increasing the variance of the measurements.

We found that the AIC varied in a motion pattern-dependent manner by means of simulation. The correlation between WM volume and motion score was positive in the step-wise and peak-wise motion, while negative in the random motion. This may be attributed to distinct artifact characteristics at GM/WM boundary caused by different motion patterns. Some ringing artifacts may create localized signal voids or hyperintensities that mimic or obscure GM/WM boundary. In addition, motion artifacts may also lead to sub-optimal registration and bias field correction, thus affecting the segmentation accuracy and contributing to AIC.

We found a significant reduction in GM volume and a significant increase in WM volume with increased motion severities in real images (Fig. 9), consistent with previous findings [10–15]. These correlations were weaker than those between simulated AIC and motion due to inter-subject variability in motion patterns. Most motion patterns of the motion scans belonged to step-wise motion, which may explain the positive correlation in WM volume.

The AIC estimated from the simulated motion-affected images of different subjects (dSimu) also exhibited consistencies with the measured AIC estimated from real motion scan (Fig. 8). However, such consistencies were lower than Simu, which may be due to different head positions and different shapes of brain structures across subjects. The advantage of dSimu is its applicability to subjects with a high incidence of motion, for whom high-quality artifact-free images are often not available.

We found that the fluctuations of FatNav-estimated motion parameters (mean rSD $\leq 0.032°$ and 0.037 mm) were several times smaller than the imaging resolution, suggesting that the FatNav can provide an accurate estimate of head position changes. However, there may be measurement errors due to limited temporal resolution of FatNav (~ 0.4 Hz), especially in the presence of fast and abrupt motion. This may be resolved in future by

reacquisition of k-space data when the estimated motion is greater than a certain motion threshold.

The current study has the following limitations: first, our simulations only consider effects of motion-induced k-space coordinate and phase changes. There are other mechanisms that might also contribute to motion artifacts, including the coil sensitivity map [31, 32], B_1 field [35], and local B_0 field changes [33, 34], and gradient non-linearities [36]. Second, the performance of dSimu might be further improved if the baseline artifact-free images are first aligned to the motion-affected images using non-rigid registration. Third, the present study employed pseudo-random k-space undersampling pattern and the SPIRiT algorithm to fill the unsampled k-space positions. It remains unclear how well the results can be generalized to new sampling patterns and reconstruction algorithms, such as parallel imaging and GRAPPA. Fourth, although Simu 3–4 can reproduce the artifacts and AIC more accurately, they entail storage of larger amounts of data and much higher computational cost than the other two approaches. Furthermore, motion parameters are needed for artifact simulation, which are often not available in clinical studies due to the lack of motion tracking techniques.

Conclusions

Our study found superior performance of simulation based on multi-channel complex k-space-data compared to simulation based on channel-combined magnitude images, and comparable performance of two different motion introduction strategies, MCP and MDV, in reproducing artifacts and AICs. Motion-induced systematic biases in brain morphometric parameters varied linearly with motion severity in a motion pattern-dependent manner.

Supplementary Information The online version contains supplementary material available at https://doi.org/10.1007/s10334-025-01246-2.

Data and code availability statements Data will be made available on reasonable request. The motion artifact simulation code is publicly available at https://gitee.com/mrphysics/Motion_Artifact_Simulation_Position_Effect and the example data are available at https://pan.baidu.com/s/1BjZaf36oMYqYKzB9-_D_Zw?pwd=ctvm.

Declarations

Conflict of interest The authors have no conflict of interest to declare.

Ethical standards This study has been approved by the ethics committee at ShanghaiTech University and has therefore beenperformed in accordance with the ethical standards laid down in the 1964 Declaration of Helsinki and its later amendments.

References

1. Johnson PM, Drangova M (2019) Conditional generative adversarial network for 3D rigid-body motion correction in MRI. Magn Reson Med 82(3):901–910
2. Haskell MW et al (2019) Network Accelerated Motion Estimation and Reduction (NAMER): convolutional neural network guided retrospective motion correction using a separable motion model. Magn Reson Med 82(4):1452–1461
3. Duffy BA et al (2021) Retrospective motion artifact correction of structural MRI images using deep learning improves the quality of cortical surface reconstructions. Neuroimage 230:117756
4. Pawar K, Chen Z, Shah NJ, Egan GF (2022) Suppressing motion artefacts in MRI using an Inception-ResNet network with motion simulation augmentation. NMR Biomed 35(4):e4225
5. Levac B, Kumar S, Kardonik S, Tamir JI (2022) FSE compensated motion correction for MRI using data driven methods. Medical image computing and computer assisted intervention MICCAI. Springer Nature Switzerland, Cham
6. Zhao B, Zhou Y, Zong X (2024) Effects of prospective motion correction on perivascular spaces at 7T MRI evaluated using motion artifact simulation. Magn Reson Med 92(3):1079–1094
7. Zahneisen B, Keating B, Singh A, Herbst M, Ernst T (2016) Reverse retrospective motion correction. Magn Reson Med 75(6):2341–2349
8. Olsson H et al (2024) Simulating rigid head motion artifacts on brain magnitude MRI data–Outcome on image quality and segmentation of the cerebral cortex. PLoS ONE 19(4):e0301132
9. Preboske GM, Gunter JL, Ward CP, Jack CR (2006) Common MRI acquisition non-idealities significantly impact the output of the boundary shift integral method of measuring brain atrophy on serial MRI. Neuroimage 30(4):1196–1202
10. Blumenthal JD, Zijdenbos A, Molloy E, Giedd JN (2002) Motion artifact in magnetic resonance imaging: implications for automated analysis. Neuroimage 16(1):89–92
11. Reuter M, Tisdall MD, Qureshi A, Buckner RL, van der Kouwe AJW, Fischl B (2015) Head motion during MRI acquisition reduces gray matter volume and thickness estimates. Neuroimage 107:107–115
12. Alexander-Bloch A et al (2016) Subtle in-scanner motion biases automated measurement of brain anatomy from in vivo MRI. Hum Brain Mapp 37(7):2385–2397
13. Igata N et al (2017) Utility of real-time prospective motion correction (PROMO) for segmentation of cerebral cortex on 3D T1-weighted imaging: Voxel-based morphometry analysis for uncooperative patients. Eur Radiol 27(8):3554–3562
14. Savalia NK, Agres PF, Chan MY, Feczko EJ, Kennedy KM, Wig GS (2017) Motion-related artifacts in structural brain images revealed with independent estimates of in-scanner head motion. Hum Brain Mapp 38(1):472–492
15. Pardoe HR, Kucharsky Hiess R, Kuzniecky R (2016) Motion and morphometry in clinical and nonclinical populations. Neuroimage 135:177–185
16. Ducharme S et al (2016) Trajectories of cortical thickness maturation in normal brain development: the importance of quality control procedures. Neuroimage 125:267–279
17. Liu S, Thung K-H, Qu L, Lin W, Shen D, Yap P-T (2021) Learning MRI artefact removal with unpaired data. Nature Mach Intell 3(1):60–67
18. Robert F, Dylan Tisdall M, Malte H, Bruce F, David HS, Kouwe AJWVD (2020) Scan-specific assessment of vNav motion artifact mitigation in the HCP Aging study using reverse motion correction, in In Proceedings of the 28th Annual Meeting of ISMRM. 2020: Virtual Meeting, p 0467

19. Liao S et al (2023) Fast and low-dose medical imaging generation empowered by hybrid deep-learning and iterative reconstruction. Cell Rep Med 4(7):101119
20. Gallichan D, Marques JP, Gruetter R (2016) Retrospective correction of involuntary microscopic head movement using highly accelerated fat image navigators (3D FatNavs) at 7T. Magn Reson Med 75(3):1030–1039
21. Griswold MA et al (2002) Generalized autocalibrating partially parallel acquisitions (GRAPPA). Magn Reson Med 47(6):1202–1210
22. Fessler JA, Sutton BP (2003) Nonuniform fast fourier transforms using min-max interpolation. IEEE Trans Signal Process 51(2):560–574
23. Lustig M, Pauly JM (2010) SPIRiT: Iterative self-consistent parallel imaging reconstruction from arbitrary k-space. Magn Reson Med 64(2):457–471
24. Cox RW (1996) AFNI: software for analysis and visualization of functional magnetic resonance neuroimages. Comput Biomed Res Int J 29:162–173
25. Zong X, Nanavati S, Hung SC, Li T, Lin W (2021) Effects of motion and retrospective motion correction on the visualization and quantification of perivascular spaces in ultrahigh resolution T2-weighted images at 7T. Magn Reson Med 86(4):1944–1955
26. Tisdall MD, Hess AT, Reuter M, Meintjes EM, Fischl B, van der Kouwe AJ (2012) Volumetric navigators for prospective motion correction and selective reacquisition in neuroanatomical MRI. Magn Reson Med 68(2):389–399
27. Ashburner J, Friston KJ (2005) Unified segmentation. Neuroimage 26(3):839–851
28. Collignon MF, Delaere D, Vandermeulen D, Suetens P, Marchal G (1995) Automated multi-modality image registration based on information theory. Imaging 3(1):263–274
29. Bazin PL et al (2020) Sharpness in motion corrected quantitative imaging at 7T. Neuroimage 222:117227
30. Lee S, Jung S, Jung K-J, Kim D-H (2020) Deep learning in MR motion correction: a brief review and a new motion simulation tool (view2Dmotion). Investig Magn Reson Imaging 24(4):196
31. Bammer R, Aksoy M, Liu C (2007) Augmented generalized SENSE reconstruction to correct for rigid body motion. Magn Reson Med 57(1):90–102
32. Yarach U, Stucht D, Godenschweger F, Speck O (2015) The correction of motion-induced coil sensitivity miscalibration in parallel imaging with prospective motion correction. In: International Society for Magnetic Resonance in Medicine (ISMRM)
33. Yarach U, Luengviriya C, Stucht D, Godenschweger F, Schulze P, Speck O (2016) Correction of B 0-induced geometric distortion variations in prospective motion correction for 7T MRI. Magn Reson Mater Phys Biol Med 29(3):319–332
34. Sulikowska A, Wharton S, Glover PM, Gowland PA (2014) Will field shifts due to head rotation compromise motion correction. In: International Society for Magnetic Resonance in Medicine (ISMRM)
35. Bammer R, Zhang B, Deng W, Wiggins GC, Stenger AV, Sodickson DK (2010) Impact of motion on parallel transmission. In: International Society for Magnetic Resonance in Medicine. (ISMRM)
36. Yarach U et al (2015) Correction of gradient nonlinearity artifacts in prospective motion correction for 7T MRI. Magn Reson Med 73(4):1562–1569